Evolution of conditionally-averaged second order structure functions in a transitional boundary layer

H. Yao*

Department of Aeronautics, Imperial College London, London SW7 2AZ, UK

F. Alves Portela†

School of Engineering Sciences, University of Southampton, Southampton, SO17 1BJ, UK

G. Papadakis‡

Department of Aeronautics, Imperial College London, London SW7 2AZ, UK

(Dated: August 28, 2020)

Abstract

We consider the bypass transition in a flat plate boundary layer subject to free-stream turbulence and compute the evolution of the second-order structure function of the streamwise velocity, $\langle du^2 \rangle(\vec{x}, \vec{r})$, from the laminar to the fully turbulent region using DNS. In order to separate the contributions from laminar and turbulent events at the two points used to define $du(\vec{x}, \vec{r})$, we apply conditional sampling based on the local instantaneous intermittency, τ (1 for turbulent and 0 for laminar events). Using $\tau(\vec{x}, t)$, we define two-point intermittencies, $\gamma^{(TT)}$, $\gamma^{(LL)}$ and $\gamma^{(TL)}$ which physically represent the probabilities that both points are in turbulent or laminar patches, or one in turbulent and the other in a laminar patch, respectively. Similarly, we also define the conditionally-averaged structure functions, $\langle du^2 \rangle^{(TT)}$, $\langle du^2 \rangle^{(LL)}$ and $\langle du^2 \rangle^{(TL)}$ and decompose $\langle du^2 \rangle(\vec{x}, \vec{r})$ in terms of these conditional averages. The derived expressions generalise existing decompositions of single-point statistics to two-point statistics. It is found that in the transition region, laminar streaky structures maintain their geometrical characteristics in the physical and scale space well inside the transition region, even after the initial break down to form turbulent spots. Analysis of the $\langle du^2 \rangle^{(TT)}$ fields reveal that the outer mode is the dominant secondary instability mechanism. Further analysis reveals how turbulence spots penetrate the boundary layer and approach the wall. The peaks of $\langle du^2 \rangle^{(TT)}$ in scale space appear in larger streamwise separations as transition progresses and this is explained by the strong growth of turbulent spots in this direction. On the other hand, the spanwise separation where the peak occurs remains relatively constant and is determined by the initial inception process. We also analyse the evolution of the two-point intermittency field, $\gamma^{(TT)}$, at different locations. In particular, we study the growth of the volume enclosed within an iso-surface of $\gamma^{(TT)}$ and notice that it increases in both directions, with the growth in the streamwise direction being especially large. The evolution of these conditional two-point statistics sheds light into the transition process from a different perspective and complements existing analyses using single-point statistics.

* hy3717@ic.ac.uk

† f.alves-portela@soton.ac.uk

‡ Corresponding author, g.papadakis@ic.ac.uk

I. INTRODUCTION

Boundary layer transition affects the performance of many engineering devices. For example, in aeronautical applications, it increases friction drag, thereby increasing fuel costs and the emission of harmful pollutants to the environment. When the disturbances are relatively strong, e.g. high turbulent intensity in the free-stream (larger than about $0.5-1\%$), roughness, acoustic waves, etc. the transition process bypasses the natural route of Tollmien-Schliching waves; this is called bypass transition [1].

In the present paper, we consider bypass transition due to free-stream turbulence, which has been studied extensively through experiments [2–5] and numerical simulations [6–9]. The transition starts with the penetration of low-frequency free-stream modes inside the boundary layer, while the high-frequency ones remain outside due to shear sheltering [10, 11]. Forward (high-speed) and backward (low-speed) streaks are then formed, which were called Klebanoff modes by Kendall [2, 12]. The mechanism of streaks formation can be explained by Rapid Distortion Theory [13]. The strong streamwise amplification is due to the lift-up effect (see [14] for a review and refer also to Landahl [15] for a description on how streaks are generated through a vortex tilting process). Mathematically, in the context of bypass transition, it is more appropriate to explain the growth as the resonant solution of the Squire equation for the wall normal vorticity when forced by the continuous Orr-Sommerfeld modes that have sinusoidal shape and reside in the free-stream (see [16] for more details and the perspective review [17] that summarises the different points of view for streak formation and growth).

The streaky structures evolve as they propagate downstream; the low-speed ones lift up to the edge of the boundary layer, interacting with high-frequency modes in the free-stream. Secondary instability occurs due to this interaction, causing turbulent spots, which eventually lead to breakdown to turbulence [6]. This process is explored in [18] who describe the streak breakdown from a three-dimensional perspective (sinuous secondary instability). More recently, Vaughan and Zaki [19] used Floquet theory to analyse idealised unsteady streaks that appear inside the boundary layer when forced by monochromatic (i.e. single frequency) modes. They found that the Kelvin-Helmholtz-type secondary instability is of two types; 'outer' or 'inner'. In a follow up work, Hack and Zaki [20], successfully predict the localized secondary instability of particular streaks under broadband free-stream forcing.

Intermittent turbulent spots appear after the break down of the laminar streaky structures. The first description of turbulent spots appeared in the experimental work of Emmons [21]. Following on from this early work, artificially generated spots were studied by experimentalists in visualization studies [22–24]. Anthony et al. [25] explored turbulent spots in bypass transition, showing that spots due to free-stream turbulence have differences from the conventional spots (spots in Emmons' experiment [21]). More recently, a numerical study of turbulent spots in bypass transition was done by Wu et al. [26]. Hairpin packets were found first before streaks, and then the packets directly lead to the formation of turbulent spots. Using conditional sampling, Nolan and Zaki [27] studied the growth of turbulent spots in terms of propagation rate and size under different external pressure gradients. Further research by Marxen and Zaki [28] examined the intermittent turbulence characteristics in the bypass transition region. Both conditional- and ensemble-averaging were used to study the intermittent turbulence spots. They found that in the core region of the spots, first and second order statistics are similar to those of a fully turbulent flow.

Most of the aforementioned work has focused on one-point statistics, i.e. the distribution of mean velocities, normal and shear stresses etc. As mentioned by Eckhardt [29], one of the challenging questions in transition is the emergence of the turbulent cascade. This provides the motivation to employ two-point statistics in order to investigate the transition process. Previous two-point analyses have employed the velocity correlation function [4, 9, 30, 31]. For example, Matsubara and Alfredsson [4] investigated the streamwise velocity correlation function and found that the spanwise length scale which corresponds to the minimum of the correlation, does not vary much in the streamwise direction. The detailed behaviour is dependent on the grid used to generate the free-stream turbulent, in some cases it increases, in other decreases. On the other hand, when scaled with the displacement thickness of the boundary layer, δ^*, it approaches a constant value, approximately $3\delta^*$ for all cases. They found also that the streaks have a streamwise length scale, which increases along the downstream direction. In the DNS of transition due to high intensity free-stream turbulence of [9], the evolution of velocity correlation function was also found to be case dependent. For the case with small turbulence length scale at the inlet, which is more similar to the one examined in this paper, the spacing of streaks (in physical units) was found to slowly increase along the downstream distance. On the other hand, when normalised with δ^*, it decays slowly; values close to $2\delta^*$ are reported. Theoretical analysis using optimal perturbation

theory applied to the Navier-Stokes equations linearised around the Blasius velocity profile [32, 33], show that the maximum amplification is found for a spanwise wavenumber β^*, that scales with δ^* as $\beta^*\delta^* = 0.77$. This corresponds to a minimum in the correlation function located at $4.08\delta^*$, thus it is expected to grow as $\sim x^{1/2}$ when expressed in physical units. In the experiments and DNS, the growth is generally found to be slower, which maybe due to the nonlinear effects induced by transition. The experiments of [3] also indicate slower growth.

In this paper, instead of using two-point velocity correlation functions, we employ the second-order structure function for the fluctuation of the streamwise velocity, u. This is a two-point statistical quantity, defined as $\langle du^2 \rangle = \langle (u^+ - u^-)^2 \rangle$, where the superscripts $^+$ and $^-$ indicate two points in space. Their coordinates are defined using the mid-point $\vec{X} = (X, Y, Z)$ and the separation vector $\vec{r} = (r_1, r_2, r_3)$, i.e. $\vec{x}^{\pm} = \vec{X} \pm \vec{r}/2$. Similar to the velocity correlation, $\langle du^2 \rangle$ is also a six-dimensional quantity, $\langle du^2 \rangle(X, Y, Z, r_1, r_2, r_3)$. We prefer however to work with the second-order structure function, as opposed to two-point correlation, for the following reasons:

(1) There is no loss of information, because there is a direct relationship between these two-point statistical quantities, $\langle du^2 \rangle = \langle (u^+ - u^-)^2 \rangle = \langle (u^+)^2 \rangle + \langle (u^-)^2 \rangle - 2\langle u^+ u^- \rangle$; the last term is the velocity correlation function.

(2) It has a more clear physical meaning, because $\langle du^2 \rangle + \langle dv^2 \rangle + \langle dw^2 \rangle$ can be regarded as the scale energy in physical space, i.e. it quantifies the energy contained within an eddy of size (length scale) $|\vec{r}|$ which is centred at point $\vec{X} = (X, Y, Z)$; refer to [34] for more details on this interpretation and the caveats for small $|\vec{r}|$. In the above sum, $\langle du^2 \rangle$ has the highest contribution, so this term is a good approximation of the scale energy. Since the structure function is formulated in physical space, it is applicable to spatially varying flows.

(3) Its transport equation is the generalized Karman-Howarth equation [35, 36], which has been increasingly used as a statistical tool for the analysis of inter-scale energy transfer in inhomogeneous and anisotropic flows, for example channel flow [37], flow around a square prism [38], and in the wake of a fractal grid [39].

Additionally, since we are studying a transitional flow, it is of interest to analyse the effect of intermittency on the statistics of $\langle du^2 \rangle$ via conditional sampling. Although this approach has long been applied to single-point statistics [40], we could not find a similar analysis for two-point statistics in the literature. We therefore derive the relevant equations and study

the conditionally averaged fields. As will be shown, many interesting physical features of transition can be elucidated from the analysis of these fields.

The paper is organised as follows. In the next section II, we briefly describe the numerical method and show comparison with reference results from the literature (computational or experimental) for validation purposes. We then proceed in section III to derive the decomposition of conditionally-averaged $\langle du^2 \rangle$. In section IV we analyse $\langle du^2 \rangle$ in the laminar and fully turbulent regions, and in section V the evolution of the conditionally-averaged fields in the transitional region. In section VI we study the two-point intermittency field $\gamma^{(TT)}$, and finally we conclude in section VII.

II. NUMERICAL METHOD AND ONE-POINT STATISTICS (VALIDATION T3A CASE)

The DNS simulation was performed using our in-house finite volume solver, Pantarhei, a finite volume solver for the Navier-Stokes equations that employs the fractional step method to enforce the continuity equation and update pressure at every time step. For more details and applications of the solver to various transitional and fully turbulent flows refer to [38, 41–43].

The spatial coordinates are normalized by the Blasius similarity variable, $L_0 = \sqrt{\nu X_0/U_\infty}$, where X_0 is the distance of the domain inlet from the leading edge of the plate. The computational domain size is $3000 \times 200 \times 150$ in the streamwise (X), wall-normal (Y) and spanwise (Z) directions respectively. The number of cells in each direction are $2049 \times 192 \times 169$. The mesh is uniform in the streamwise and spanwise directions, while in the wall-normal direction the cells grow with expansion ratio 1.06 until $Y = 20L_0$; further away from the wall the mesh is uniform. The resulting spacings in wall units (indicated by $^+$) are $\Delta x^+_{max} \sim 11.78$, $\Delta y^{+(w)}_{max} \sim 0.24$, and $\Delta z^+_{max} \sim 7.14$. The subscript max denotes maximum values (found in the fully turbulent region), while $\Delta y^{+(w)}_{max}$ is evaluated at the centroid of the first cell close to the wall. The inlet Reynolds number is $Re_{L_0} = 160$.

We let the flow develop for sufficiently long time to reach statistically steady state and then collect statistics for 3 flow-through times. The time step is set to $0.2T_0$ (where $T_0 = L_0/U_\infty$), which results in a maximum CFL number of around 0.35. Two-point statistics are calculated from 350 samples with time and spanwise averaging. The time separation

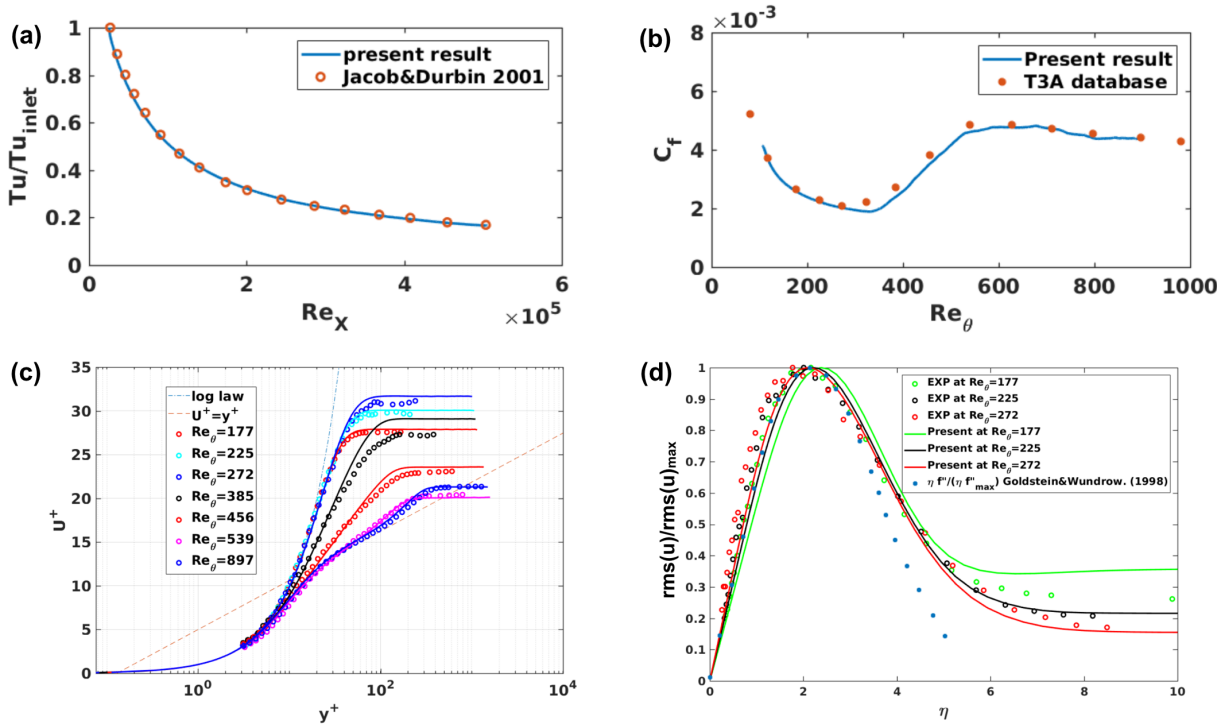

FIG. 1. (a) Free-stream turbulent intensity, Tu against Re_x; (b) Skin friction coefficient, C_f, against Re_θ; (c) Mean streamwise velocity, U^+ against y^+; (d) $rms(u)/rms(u)_{max}$ against the Blasius variable, η.

between two samples is $20T_0$, i.e. we sample every 100 time steps. Convergence is reported in Figure 18 of Appendix A where $\langle du^2 \rangle$ is plotted against the number of samples at a fixed streamwise position (located in the turbulent region) and wall-normal distance, for small and large streamwise separations r_1 (and $r_3 = 0$). It can be seen that after about 200 samples, the average has reached a converged value. Similar results are found at other streamwise positions, wall-normal locations and separations.

The free-stream turbulent intensity, Tu, is set to 3.4% to match the transition onset location; this is close to the value of 3.5% of Jacob and Durbin [6]. The Von Karman spectrum

$$E(k) = Tu^2 \frac{1.196(kL_{11})^4}{[0.558 + (kL_{11})^2]^{17/6}} L_{11}, \quad Tu = 3.4\%, \quad L_{11} = 5L_0 \tag{1}$$

is assumed for the turbulent fluctuations in the free-stream. The length scale is set to $L_{11} = 5L_0$, which is approximately equal to the boundary layer thickness at the inlet.

For the generation of the inlet conditions that satisfy the aforementioned spectrum, we follow a process similar to previous DNS simulations [7]. To check the implementation of

the inlet conditions, in panel (a) of Fig. (1) we compare the decay rate of the free-stream turbulence intensity against the results of Jacob and Durbin [6]; we notice that the two sets of results match well. The skin friction coefficient, C_f, against the momentum thickness, Re_θ, also matches well with the T3A experiments [44], as shown in panel (b) of Fig. (1). There is a small deviation for $250 < Re_\theta < 350$, where the current result is slightly lower than the experimental data. In Jacob's work, the C_f is slightly overestimated (refer to fig.4 in [6]).

In panel (c) we compare the mean streamwise velocity (in wall units) against the T3A experiment [44]. In the late transition and fully turbulent region the matching is good, however, the mean velocity in the transition region is more difficult to match. This is due to differences in the free-stream conditions that are very difficult to reproduce exactly. Panel (d) displays the profile of $rms(u)/rms(u)_{max}$ against the Blasius variable, η. The circles are calculated using the raw data from the T3A database [44]. The profile matches well (up to $\eta \approx 4$) with the normalised shape of $\eta F''$, where F'' is the Blasius function. The latter formula was originally used by Taylor [45] and Klebanoff [2] for experimental data fitting. The streamwise velocity fluctuation profile clearly indicates the presence of the so-called Klebanoff modes.

It is instructive at this point to visualise some instantaneous velocity fields. In the left panels of Fig. (2), we use the instantaneous wall-normal fluctuation velocity, v, to visualise turbulent structures (spots) at $Y/L_0 = 5$. A large, fully formed structure can be seen on the right of the top left panel. Note the rapid change of the sign of v over the structure. A smaller structure, just forming, can be discerned in the area $(X - X_0)/L_0 \approx 1050 - 1100$ and $Z/L_0 \approx 25$. We track the growth of this turbulent structure at 4 time instants (left panels, from top to bottom). The growth of the structure in the streamwise and spanwise directions is evident.

In the right panels, we show contours of the instantaneous streamwise velocity fluctuations through the centre of the spot, at the same time instants. The horizontal domain visualised in the right panels is shifted in the streamwise direction in order to account for the translating motion of the structure; the domain shown corresponds to the horizontal dashed lines in the left panels. On the top right panel, we see the lifting up of the low speed streak (negative fluctuating velocities). The velocity field at this time instant is smooth, but in the panel below the footprints of secondary instability start to appear at $Y \sim 12L_0$,

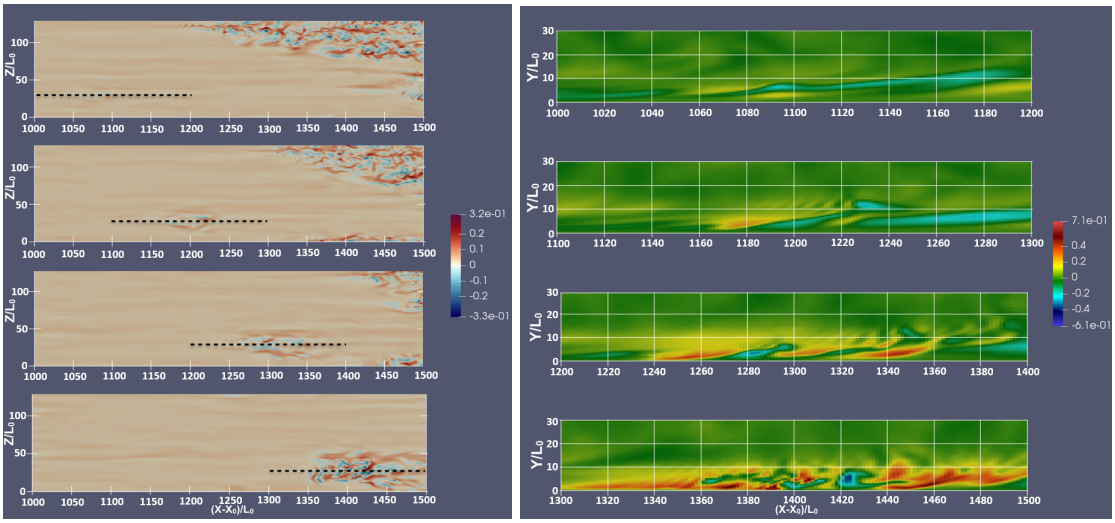

FIG. 2. Flow snapshots tracking a spot from its incipient formation (top row) to fully developed form (bottom row); wall-normal velocity fluctuations at $Y = 5L_0$ (left panels); streamwise velocity fluctuations in the plane at $Z = 25L_0$ (indicated as horizontal dash lines on the left panels) that pass through the centre of the spot (right panels). Note the translation of the domain visualised in the streamwise direction in the right panels. The time interval between each snapshot is $190L_0/U_\infty$.

$(X - X_0)/L_0 \sim 1180 - 1220$. The turbulent motion moves closer to the wall and fills the boundary layer below $10L_0$; a fully formed spot has been formed, as can be seen in the bottom row (left and right panels). The observed growth of spots cannot be captured with single-point statistics, but as will be seen later, two-point statistics, especially ones conditioned on turbulent events, is a very effective statistical tool for this purpose.

III. DERIVATION OF CONDITIONALLY-AVERAGED TWO-POINT STATISTICS

A. Binary indicator function

We define an instantaneous binary indicator function, $\tau(X, Y, Z, t)$, that takes the value 1 if the flow is turbulent and 0 if it is laminar. Similar to the work by Marxen and Zaki [28], this indicator function is based on the standard deviation of $D = |v| + |w|$, where v, w are the wall-normal and spanwise velocities respectively (using the standard deviation to detect the turbulent patches is consistent with the snapshots shown in figure 2). We also use Otsu's

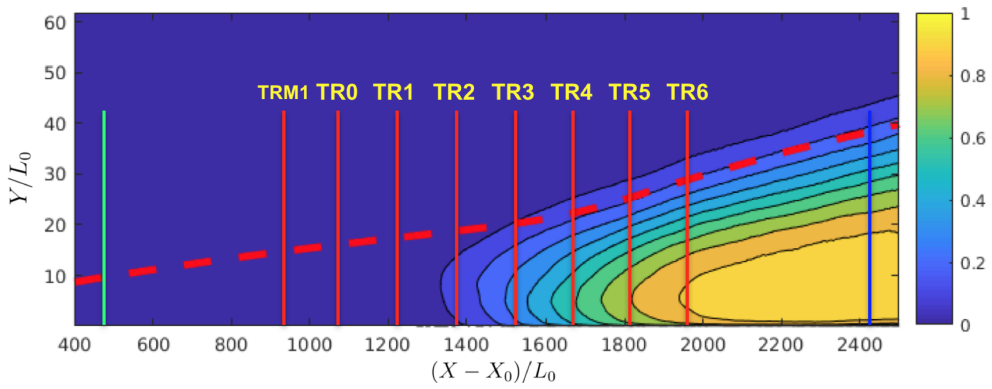

FIG. 3. Contour plot of the intermittency field γ. The red dashed line represents the boundary layer thickness. The vertical solid lines in green, red and blue represent the streamwise locations where the second-order structure functions are calculated. The green line is in the laminar region ($(X - X_0)/L_0 = 540$) and the blue in the turbulent region ($(X - X_0)/L_0 = 2415$). The eight red lines, $TRM1$ and $TR0 - TR6$ are in the transition region and their coordinates are $940, 1065, 1215, 1365, 1515, 1665, 1815, 1965$ respectively.

method [46] to find an optimal threshold to identify the turbulent and non-turbulent regions.

The time and spanwise average of the τ field

$$\gamma(X, Y) = \frac{1}{\Delta T L_z} \int_0^{\Delta T} \int_0^{L_z} \tau(X, Y, Z, t) dz dt \tag{2}$$

is known as intermittency, γ. A contour plot is shown in Fig. (3); it is very similar to Fig. (5) in [28]. By arguing that turbulent spots are born with equal probability, Narasimha [47, 48] proposed a 'universal' distribution for intermittency, which matches well with the present result of $\gamma_{max}(X) = max(\gamma(X, Y))$, as shown in Fig. (4).

The binary indicator function and the intermittency field allow us to define conditional averaged statistics, as explained in the next subsection.

B. Derivation of conditional two-point structure function

We start by first summarising existing expressions for single-point statistics. We use capital symbols, for example U_i or Φ, to denote instantaneous quantities and lower case symbols, u_i or ϕ, to denote fluctuations around a time and spanwise-averaged variable, $\langle U_i \rangle$ or $\langle \Phi \rangle$.

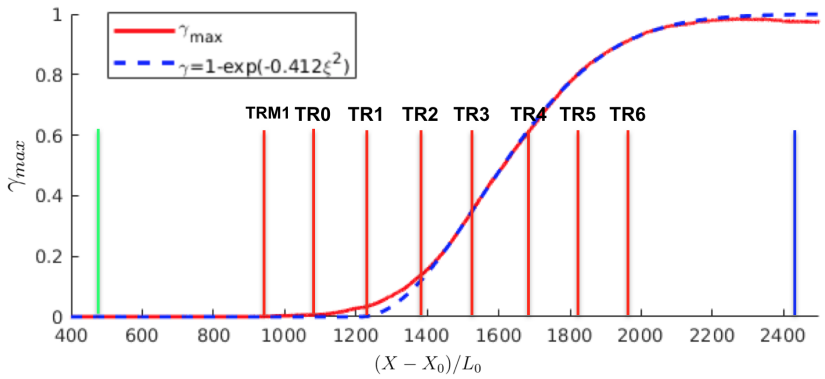

FIG. 4. Variation of γ_{max} (solid line) in the streamwise direction and comparison with the formula of Narashima (dashed line), where $\xi = (X - X_s)/(X_{\gamma=0.75} - X_{\gamma=0.25})$, and X_s is the location transition starts, taken to be at $(X_s - X_0)/L_0 = 1100$.

A conventionally averaged quantity $\langle\Phi\rangle$, can be decomposed into conditionally-averaged quantities using the intermittency γ as follows:

$$\langle\Phi\rangle = \gamma\langle\Phi\rangle^{(T)} + (1-\gamma)\langle\Phi\rangle^{(L)}, \tag{3}$$

where the superscripts (T) and (L) indicate averages conditioned on turbulent and laminar events respectively. The conditionally averaged variables are defined as,

$$\langle\Phi\rangle^{(T)} = \frac{1}{\Delta T L_z \gamma}\int_0^{\Delta T}\int_0^{L_z} \tau\Phi dz dt \qquad \langle\Phi\rangle^{(L)} = \frac{1}{\Delta T L_z (1-\gamma)}\int_0^{\Delta T}\int_0^{L_z} (1-\tau)\Phi dz dt \tag{4}$$

Using the Reynolds decomposition $\phi = \Phi - \langle\Phi\rangle$, the variance of fluctuations can be written as,

$$\langle\phi^2\rangle = \langle\Phi^2\rangle - \langle\Phi\rangle^2 \tag{5}$$

and similarly for the conditional variances,

$$\langle\phi^2\rangle^{(T)} = \langle\Phi^2\rangle^{(T)} - (\langle\Phi\rangle^{(T)})^2 \qquad \langle\phi^2\rangle^{(L)} = \langle\Phi^2\rangle^{(L)} - (\langle\Phi\rangle^{(L)})^2 \tag{6}$$

The variance can also be written in terms of conditional-averaged quantities as [40],

$$\langle\phi^2\rangle = \gamma\langle\phi^2\rangle^{(T)} + (1-\gamma)\langle\phi^2\rangle^{(L)} + \gamma(1-\gamma)(\langle\Phi\rangle^{(T)} - \langle\Phi\rangle^{(L)})^2 \tag{7}$$

We can employ the same decomposition for the time and spanwise-averaged Reynolds stresses. The latter can be written in terms of conditional-averaged quantities as [28, 40],

$$\langle u_i u_j\rangle = \gamma\langle u_i u_j\rangle^{(T)} + (1-\gamma)\langle u_i u_j\rangle^{(L)} + \gamma(1-\gamma)\left(\langle U_i\rangle^{(T)} - \langle U_i\rangle^{(L)}\right)\left(\langle U_j\rangle^{(T)} - \langle U_j\rangle^{(L)}\right) \tag{8}$$

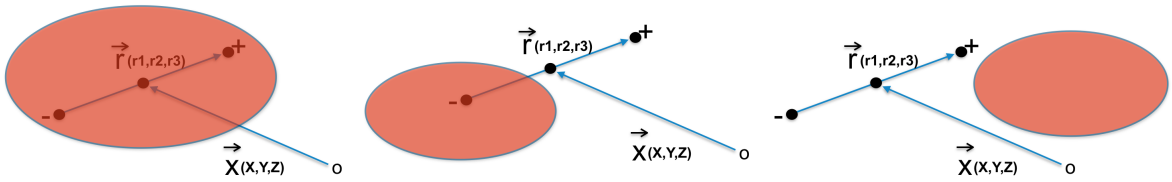

FIG. 5. Sketches of the three states. Red ovals represent turbulent spots. Both points are within a turbulent spot (state TT, left), one point inside a turbulent spot, the other in laminar region (state TL, middle), both points in the laminar region (state LL, right).

We can extend this decomposition to two-point statistics; the two points are indicated by the superscripts $^+$ and $^-$. The conditional averaging now includes three different states that are defined as,

$$\text{States} = \begin{cases} \text{Turbulent-Turbulent (TT)} & \tau^+ = 1, \tau^- = 1 \\ \text{Turbulent-Laminar (TL)} & \tau^+ = 1, \tau^- = 0 \text{ or } \tau^+ = 0, \tau^- = 1 \\ \text{Laminar-Laminar (LL)} & \tau^+ = 0, \tau^- = 0 \end{cases} \tag{9}$$

A schematic diagram for each state is shown in figure (5).

Using the identity

$$\tau^+\tau^- + \left(\tau^+(1-\tau^-) + (1-\tau^+)\tau^-\right) + (1-\tau^+)(1-\tau^-) = 1, \tag{10}$$

the instantaneous velocity difference $dU = U^+ - U^-$ can be written as,

$$dU = \tau^+\tau^- dU + \left(\tau^+(1-\tau^-) + (1-\tau^+)\tau^-\right) dU + (1-\tau^+)(1-\tau^-)dU \tag{11}$$

Taking the time and spanwise average of the above equation, we get the following decomposition,

$$\langle dU \rangle = \gamma^{(TT)}\langle dU \rangle^{(TT)} + \gamma^{(TL)}\langle dU \rangle^{(TL)} + \gamma^{(LL)}\langle dU \rangle^{(LL)} \tag{12}$$

where

$$\begin{aligned} \langle dU \rangle^{(TT)} &= \frac{1}{\Delta T L_z \gamma^{(TT)}} \int_0^{\Delta T}\int_0^{L_z} \tau^+\tau^-(U^+ - U^-)dzdt \\ \langle dU \rangle^{(TL)} &= \frac{1}{\Delta T L_z \gamma^{(TL)}} \int_0^{\Delta T}\int_0^{L_z} \left(\tau^+(1-\tau^-) + (1-\tau^+)\tau^-\right)(U^+ - U^-)dzdt \\ \langle dU \rangle^{(LL)} &= \frac{1}{\Delta T L_z \gamma^{(LL)}} \int_0^{\Delta T}\int_0^{L_z} (1-\tau^+)(1-\tau^-)(U^+ - U^-)dzdt \end{aligned} \tag{13}$$

are the conditional averages and,

$$\begin{aligned}
\gamma^{(TT)} &= \frac{1}{\Delta T L_z}\int_0^{\Delta T}\int_0^{L_z} \tau^+\tau^- dzdt, \\
\gamma^{(TL)} &= \frac{1}{\Delta T L_z}\int_0^{\Delta T}\int_0^{L_z} (\tau^+(1-\tau^-)+(1-\tau^+)\tau^-) dzdt, \\
\gamma^{(LL)} &= \frac{1}{\Delta T L_z}\int_0^{\Delta T}\int_0^{L_z} (1-\tau^+)(1-\tau^-) dzdt,
\end{aligned} \tag{14}$$

are the two-point intermittencies; the latter generalise equation (2). Due to the identity (10), their sum is

$$\gamma^{(TT)} + \gamma^{(TL)} + \gamma^{(LL)} = 1. \tag{15}$$

The definition (14) indicates that $\gamma^{(TT)}, \gamma^{(TL)}, \gamma^{(LL)}$ can be physically interpreted as probabilities. For example, $\gamma^{(TT)}$ is the probability that both points $\vec{x}^{\pm}$ are located within turbulent patches; similar interpretations can be given to $\gamma^{(TL)}$ and $\gamma^{(LL)}$. The sum of the probabilities is equal to 1 (equation 15) and (12) is a weighted sum that involves the probabilities of the three states and the corresponding conditional averages.

Similar to the single-point case, the variance and conditional variance for the fluctuations difference can be written as,

$$\begin{aligned}
\langle du^2\rangle = \langle dU^2\rangle - \langle dU\rangle^2 \qquad & \langle du^2\rangle^{(TT)} = \langle dU^2\rangle^{(TT)} - (\langle dU\rangle^{(TT)})^2 \\
\langle du^2\rangle^{(TL)} = \langle dU^2\rangle^{(TL)} - (\langle dU\rangle^{(TL)})^2 \qquad & \langle du^2\rangle^{(LL)} = \langle dU^2\rangle^{(LL)} - (\langle dU\rangle^{(LL)})^2
\end{aligned} \tag{16}$$

Using equations (12) and (16) and after some algebra, we obtain the following decomposition of $\langle du^2\rangle$

$$\langle du^2\rangle = \gamma^{(TT)}\langle du^2\rangle^{(TT)} + \gamma^{(TL)}\langle du^2\rangle^{(TL)} + \gamma^{(LL)}\langle du^2\rangle^{(LL)} + \Psi\left(\langle dU\rangle^{(TT)}, \langle dU\rangle^{(TL)}, \langle dU\rangle^{(LL)}\right) \tag{17}$$

where,

$$\begin{aligned}
\Psi\left(\langle dU\rangle^{(TT)}, \langle dU\rangle^{(TL)}, \langle dU\rangle^{(LL)}\right) =& \gamma^{(TT)}(\langle dU\rangle^{(TT)})^2 + \gamma^{(TL)}(\langle dU\rangle^{(TL)})^2 + \gamma^{(LL)}(\langle dU\rangle^{(LL)})^2 \\
& - (\gamma^{(TT)}\langle dU\rangle^{(TT)} + \gamma^{(TL)}\langle dU\rangle^{(TL)} + \gamma^{(LL)}\langle dU\rangle^{(LL)})^2
\end{aligned} \tag{18}$$

The above equation generalises the existing decomposition of single-point statistics, equation (7), to two-point ones. We checked its validity by performing numerical experiments with synthetic data.

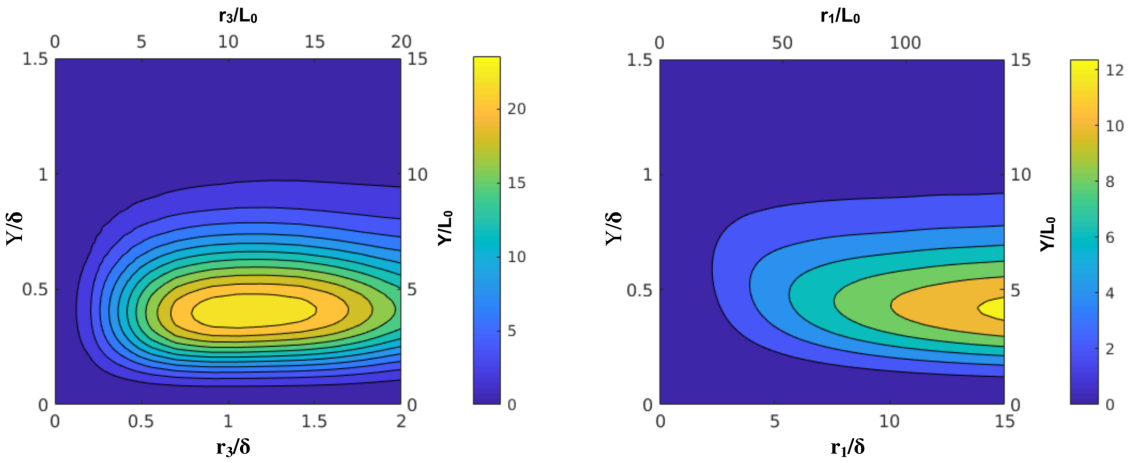

FIG. 6. $\langle du^2 \rangle$ on (r_3, Y) (left) and (r_1, Y) (right) planes in the laminar region. Note that left and bottom axes are normalised by the local boundary layer thickness (δ), while top and right axes are normalised by the inlet Blasius similarity variable, L_0.

IV. TWO-POINT STRUCTURE FUNCTION IN LAMINAR AND TURBULENT REGION

In this section, contour plots of the time- and spanwise- averaged streamwise structure functions are presented on (r_3, Y) and (r_1, Y) planes at the streamwise locations X_i shown as vertical solid lines in Fig. (3). For each plane, we consider that the other separations are 0. For example, in the (r_1, Y) plane we plot $\langle du^2 \rangle (r_1, Y; X_i, r_2 = 0, r_3 = 0)$, while for the (r_3, Y) plane we plot $\langle du^2 \rangle (r_3, Y; X_i, r_1 = 0, r_2 = 0)$. For all plots, the values are normalised by the square of the local friction velocity, $u_\tau^2(X_i)$.

The conventionally averaged $\langle du^2 \rangle$ is first plotted in the laminar and turbulent regions. This is followed by similar plots in the transitional region, and finally we present the maps of conditionally averaged quantities.

A. Streaky laminar region

The structure function in the streaky laminar region, corresponding to the green line in Fig. (3), is shown in Fig. (6). Note that the separations in the spanwise and streamwise directions as well as the wall-normal distance are normalised by two scales; one local (boundary layer thickness, δ) and one global (inlet Blasius variable, L_0).

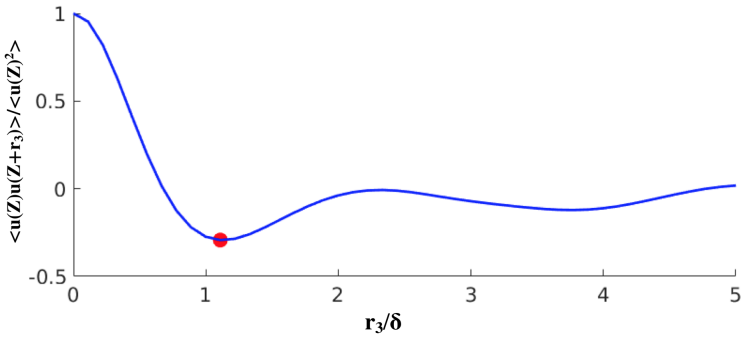

FIG. 7. Second-order streamwise velocity correlation function with respect to spanwise separation at wall-nornal distance $Y_0 \sim 4L_0$.

A clear peak can be observed in the $\langle du^2 \rangle$ on (r_3, Y) plane as shown in the left panel of Fig. (6). The peak corresponds to $r_3 \approx 1.1\delta$ (or $r_3 \approx 3\delta^*$, or $r_3 \approx 10 - 11L_0$ in global units). As mentioned in the introduction, in the homogeneous direction, $\langle du^2 \rangle = 2\left(\langle u^2 \rangle - \langle u^+ u^- \rangle\right)$, and due to the negative sign before the correlation term, the minimum in the $\langle u^+ u^- \rangle$ corresponds to a maximum of structure function. This distance is the average spacing between laminar high and low speed streaks. The value of $r_3 \approx 1.1\delta$ matches the location of the first minimum point of the streamwise two-point velocity correlation function (red spot in Fig. (7)). When normalised with the displacement thickness, the value of $\approx 3\delta^*$ is within the region reported in experimental and numerical theoretical studies [4, 9], but smaller compared to $4.08\delta^*$, the value predicted by the optimal perturbation theory of [32, 33]. This may be related to the fact that the peak in the optimal perturbation (figure 2 in [32]) is not very sharp, and the exact value selected is determined by the imposed length scale and the intensity of the free-stream turbulence at the inlet.

The scale energy peak in the wall-normal direction is located at $Y \approx 0.4\delta$ (or $Y \approx 4L_0$). This indicates the presence of Klebanoff modes, where the largest turbulent intensity of streamwise fluctuation is located around the middle of the laminar boundary layer [4, 32]. This is also consistent with the one-point statistics shown in Fig. 1(d), i.e. peak at $\eta \approx 2.2$ (with thickness $\eta \approx 5$).

The right panel of figure (6) shows the structure function on the (r_1, Y) plane. The largest values are also located at $Y \approx 0.4\delta$ as expected, but $\langle du^2 \rangle$ grows continuously with the streamwise separation r_1, even until the maximum value considered, $r_1 = 15\delta$. We have examined also larger separations (plots not shown) and found that $\langle du^2 \rangle$ continues to

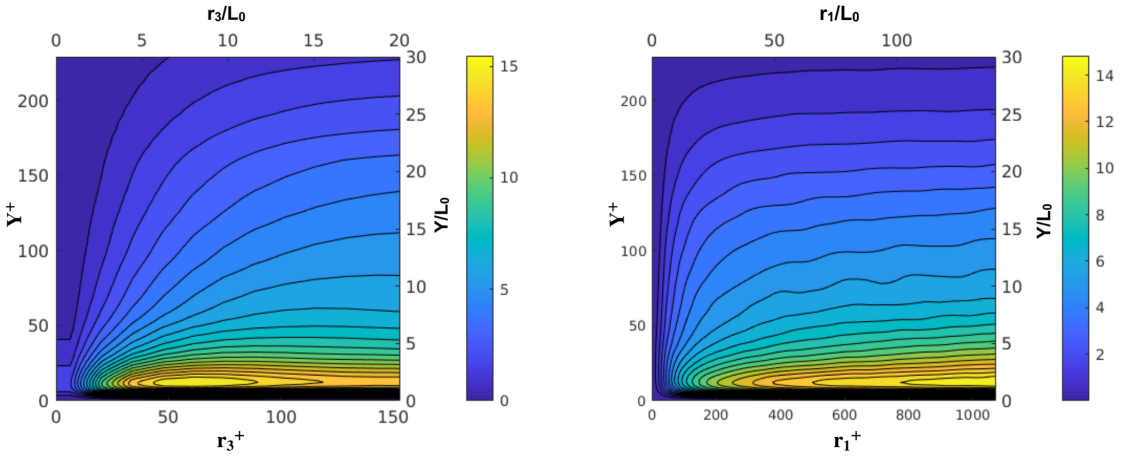

FIG. 8. $\langle du^2 \rangle$ on (r_3, Y) (left) and (r_1, Y) (right) planes in the fully turbulent region. Left and bottom axes are in local wall units, while top and right axes are in global units of L_0.

increase, but at a slower rate. We expect that at the very large r_1, the velocity fluctuations at the two points $\vec{x}^{\pm}$ will become uncorrelated and $\langle du^2 \rangle$ will tend to $\langle (u^+)^2 \rangle + \langle (u^-)^2 \rangle$. If the flow were homogeneous in the streamwise direction, then $\langle du^2 \rangle$ would tend to a constant value, equal to $2\langle u^2 \rangle$; this is nicely shown in figure 2 of [49]. In our case however, the flow has strong spatial inhomogeneity and $\langle du^2 \rangle$ continues to increase for large r_1, but at reduced rate.

B. Fully turbulent region

The structure function in the fully turbulent region corresponding to the blue line in Fig. (3) is shown in Figure (8). Again we normalise the separations and wall-normal distances using local wall units (bottom axes) as well as the global reference quantity L_0 (top axes). In the (r_3, Y) plane (left panel), a peak is found at $r_3^+ \approx 70$ and $Y^+ \approx 16$. This corresponds to the spanwise distance of the near-wall streaks and the energy peak region is located in the buffer layer. The results are very similar to the structure function calculated in channel flow [37, 50]. In terms of global units, the maximum is located at $r_3 \approx 7 - 8L_0$, while in the laminar region it was at $r_3 \approx 10 - 11L_0$. It is also closer to the wall, because the mean velocity profile has become steeper (as can be seen from the C_f coefficient) and the production takes place closer to the wall. From the (r_1, Y) plane (right panel), we can see that the structure function grows over much larger separations in the streamwise direction

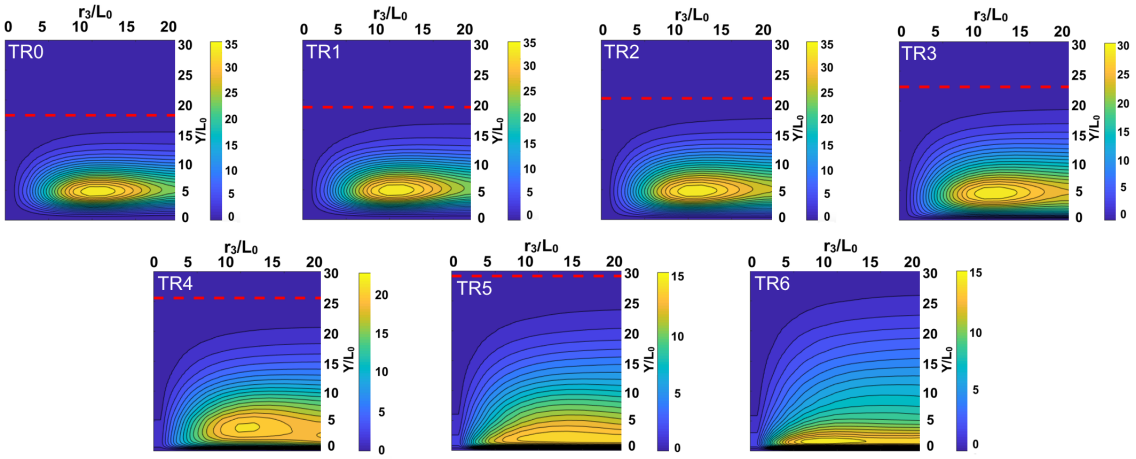

FIG. 9. Evolution of $\langle du^2 \rangle$ on (r_3, Y) plane along the streamwise direction. The locations, denoted as $TR0 - TR6$, are defined in Fig. (3). In this and all subsequent figures, the red dash line represents the local boundary layer thickness.

compared to the spanwise one; this is indicative of very long streaky structures. Again the largest values in the wall-normal direction for different separations are located within the buffer layer, at $Y^+ \approx 16$, as expected.

V. TWO-POINT STRUCTURE FUNCTION MAPS IN TRANSITIONAL REGION

In this section, we plot maps of the standard and conditionally-averaged structure functions in the transition region on the (r_3, Y) and (r_1, Y) planes, at the locations of the red lines shown in Fig. (3).

A. Evolution of the standard structure function on $(r_3/r_1, Y)$ plane

From Fig. (9), we see the morphing of the structure functions on the (r_3, Y) plane from the laminar-like to the turbulent-like shape, compare with the left panels of Figures (6) and (8) respectively. In the streamwise locations $TR0 - TR3$, the characteristics of the laminar streaks are largely retained, i.e. the peak appears at $Y \approx 5L_0$ (slightly further from the wall compared to the distance of $4L_0$ in the fully laminar regime) and $r_3 \approx 10L_0$. At later stages, however, starting from $TR4$, and more evidently in $TR5$ and $TR6$, the shape changes

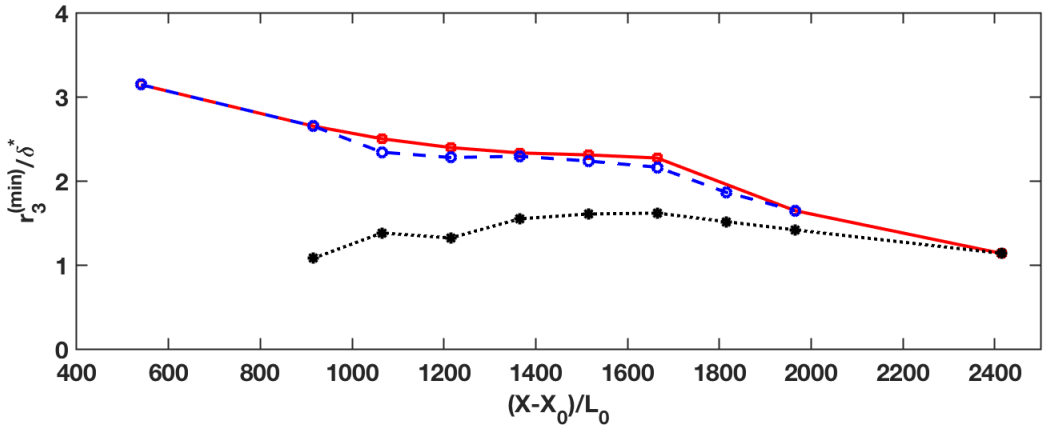

FIG. 10. Variation of the $r_3^{(min)}/\delta^*$ along the streamwise direction. The solid red line refers to the maps of $\langle du^2 \rangle$ in Fig. (9), while the blue dash and the black dotted lines refer to the maps of $\gamma^{(LL)}\langle du^2 \rangle^{(LL)}$ in Fig. (12) and $\gamma^{(TT)}\langle du^2 \rangle^{(TT)}$ in Fig. (14) respectively. Circles mark the streamwise locations of Fig. (3).

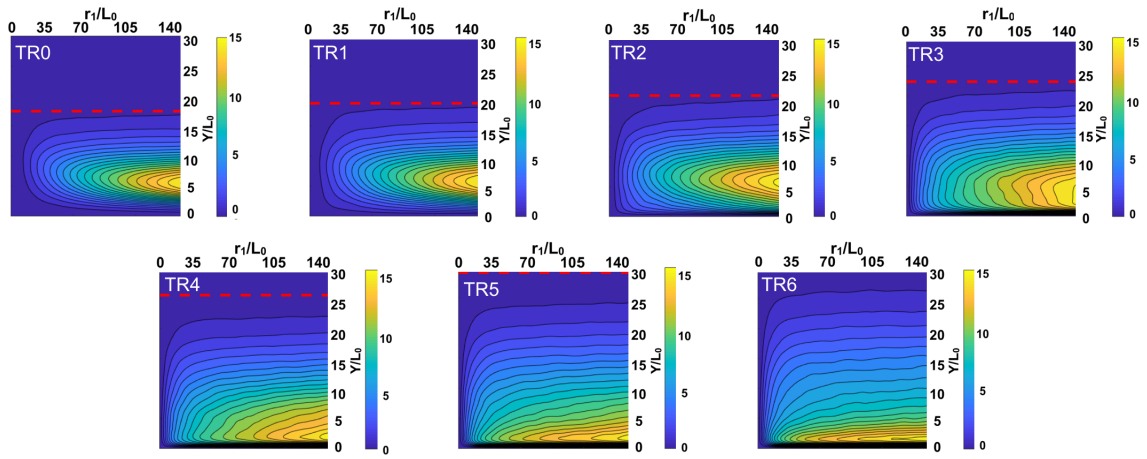

FIG. 11. Evolution of $\langle du^2 \rangle$ on (r_1, Y) plane in the transitional region.

significantly and the peak location approaches closer to the wall, $Y \approx 1.6L_0$. The spanwise location of the peak, however, is maintained up to $TR5$ and only in $TR6$ it is reduced to the turbulent value of $7 - 8L_0$.

In Fig. (10) we plot the location of the peak normalised with the displacement thickness, $r_3^{(min)}/\delta^*$ (solid red line). The values are between $2 - 3$ until the late stage of transition (location $TR4$, $(X - X_0)/L_0 \approx 1700$), and match with the numerical results of [9] (figure 12 in which $r_3^{(min)}$ tends to $2\delta^*$) and the experimental results of [4] (figure 8 in which $r_3^{(min)}$

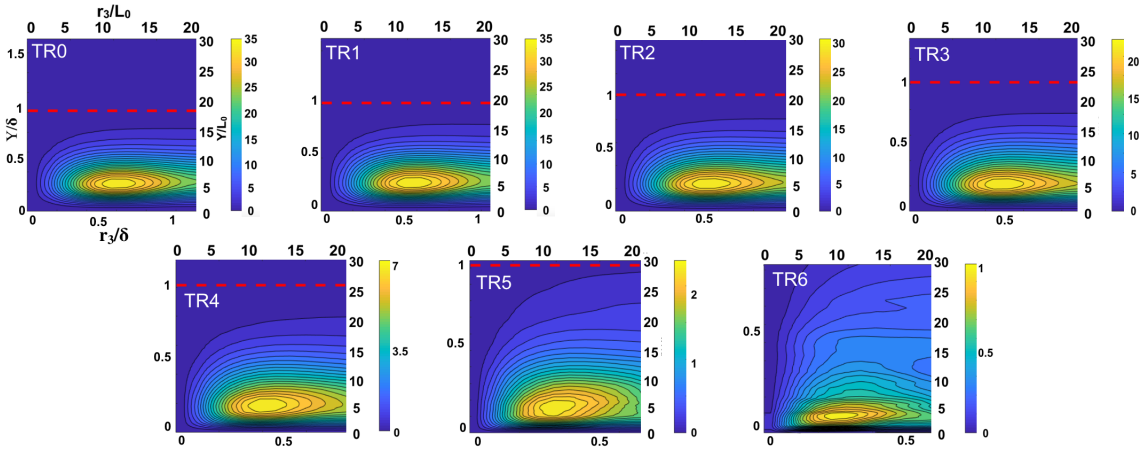

FIG. 12. Evolution of $\gamma^{(LL)}\langle du^2\rangle^{(LL)}$ on (r_3, Y) plane.

tends to $3\delta^*$). Differences might be due to the different inlet conditions of the free-stream turbulence. After $TR4$ the spacing decreases, approaching the value for the fully turbulent region.

Similar to the results on (r_3, y) plane, the structure function $\langle du^2\rangle$ on (r_1, Y) plane, shown in Fig. (11), morphs from laminar-like to turbulent-like shape. The peak of the scale energy moves from $Y \approx 5L_0$ down to $Y \approx 1.6L_0$. It appears that at $TR3$, there is an extended peak region from $Y \approx 1 - 5L_0$. This is the streamwise location where the peaks amalgamate and further downstream the bottom peak starts to dominate.

The structure functions presented above evolve smoothly between the two limiting shapes presented in the previous section IV. However standard time and spanwise averaging conceals important information. The next subsections present the evolution of conditionally averaged structure functions. As will be seen, the latter provide richer information about the transition, especially when the conditioning is based on turbulent events.

B. Evolution of structure function on $(r_3/r_1, Y)$ plane conditioned on laminar events.

The evolution of $\gamma^{(LL)}\langle du^2\rangle^{(LL)}$ is shown in figure (12). Note that we chose to plot $\gamma^{(LL)}\langle du^2\rangle^{(LL)}$, instead of $\langle du^2\rangle^{(LL)}$, because the former appears in the decomposition (17). It is evident that the laminar streaks persist throughout the transition, retaining the same spanwise length scale and peak energy location, i.e. peak at $r_3 \approx 11L_0$ and $Y \approx 5L_0$. It is

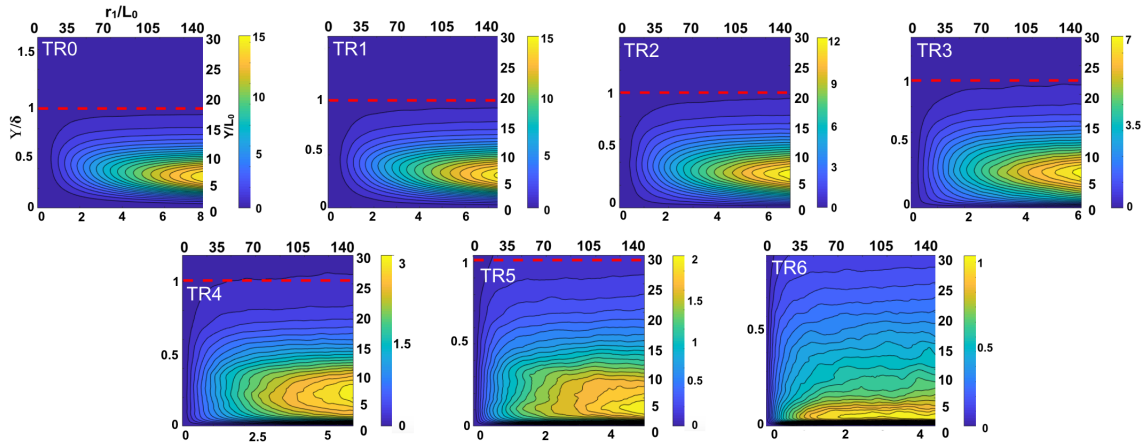

FIG. 13. Evolution of $\gamma^{(LL)}\langle du^2\rangle^{(LL)}$ on (r_1, Y) plane

also interesting to observe that the peak energy stays at $Y \approx 5L_0$, even though the boundary layer is growing (the red dash lines represent the thickness of the boundary layer). Compare for example the bottom row of figure (12) with that of figure (9); the differences at locations $TR4$ and $TR5$ are striking. In the last plot for $TR6$, the laminar characteristics become less clear and the peak of $\gamma^{(LL)}\langle du^2\rangle^{(LL)}$ decreases to $r_3 \approx 8L_0$. The plot is also less smooth compared to the other plots, because at the late stages of transition streaks start to merge with the turbulent boundary layer, thereby reducing the number of samples available for averaging conditioned on laminar events.

The variation of $r_3^{(min)}/\delta^*$ along X is also shown in Fig. (10) with dashed blue line. It is similar to the red line, i.e. the the values slowly decrease to $2.3\delta^*$, remain nearly constant, and then decrease faster (as expected due to the rapid growth of δ^*).

Similar conclusions can be made for the (r_1, Y) maps, shown in Figure 13. The laminar streaky structures retain their characteristics deep into the transition region. Indeed, compared with figure 11, we notice strong similarities for locations $TR0 - TR2$ as expected, but for $TR3$ and $TR4$ we observe significant differences; in figure 13 the shape of the latter two is much closer to the laminar shape. For $TR5$ and $TR6$ the shape becomes again similar to that shown in 11. Even though we condition on laminar events, the underlying average flow has been modified and its footprint is reflected in the $\gamma^{(LL)}\langle du^2\rangle^{(LL)}$ maps and the peak appears closer to the wall. As before, the plot for $TR6$ is not very smooth because of the reduced number of valid samples.

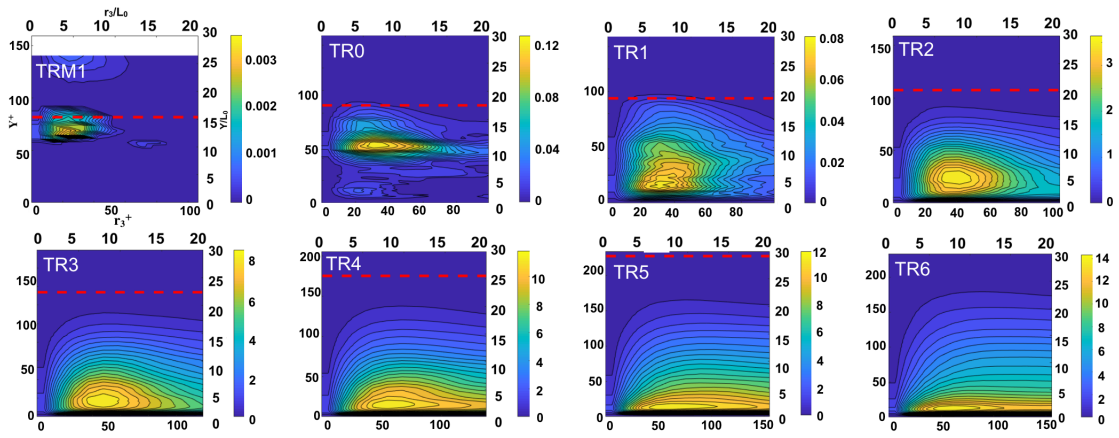

FIG. 14. Evolution of $\gamma^{(TT)}\langle du^2\rangle^{(TT)}$ on (r_3, Y) plane; their corresponding locations are $TRM1, TR0 - TR6$ shown in Fig. (3)

C. Evolution of structure function on $(r_3/r_1, Y)$ plane conditioned on turbulent events.

The maps conditioned on turbulent events are shown in Figure (14). It is very interesting to notice that, at the earliest stage of transition at location $TR0$, turbulent motions exist near the middle of the boundary layer, with a spanwise length scale $\approx 7.5L_0$. These motions can be detected only when we apply conditional averaging; indeed they are absent when we apply standard time and spanwise averaging as evidenced in figure 9. This demonstrates that the proposed conditional sampling can reveal features that would not have been possible to bring to the fore otherwise.

The presence of turbulent motions in the middle of the boundary layer at the very early stages of transition is consistent with the outer type of the secondary instability mentioned in [19]. In order to shed more light into this feature, we have considered one more location, $TRM1$, located upstream of $TR0$, as shown in figure 3. At this location, we can clearly see that the turbulent activity starts near the edge of the boundary layer, at $Y \approx 12L_0$, entirely consistent with the instantaneous pattern shown in figure 2 (second row from the top, on the right). The spanwise length scale at this earlier location is $5L_0$, exactly equal to the length scale L_{11} that we impose on the energy spectrum at the inlet, equation (1). Note also that the turbulent motions outside the boundary layer, i.e. in the free stream, are also captured, and have the imposed length scale of $L_{11} = 5L_0$.

The succession of maps also demonstrates how the turbulent motions that were initiated

at the top of the boundary layer, penetrate deep inside it and approach the wall quite early, even at $TR1$ and more clearly in $TR2$. These near-wall coherent structures (turbulent spots) become more visible at the late-stages of transition $TR4 - TR6$.

It is very instructive to compare figures 12 and 14 that show $\gamma^{(LL)}\langle du^2\rangle^{(LL)}$ and $\gamma^{(TT)}\langle du^2\rangle^{(TT)}$ respectively in the (r_3, Y) plane. When conditioning on laminar events, the peak is located at separation $r_3 \approx 10$ at all positions $TR0 - TR6$; as already mentioned, this is very close to the peak observed in the laminar state, see left panel of figure 6. When conditioning however on turbulent events, the location moves to $r_3 \approx 7 - 8$ at all streamwise positions, very close to the peak for the fully turbulent state, see left panel of figure 8. The two states, therefore, coexist during the whole transition process, and most importantly both retain their structural and geometric features that are determined at their inception. For the laminar state, the inception of Klebanoff modes is determined by the receptivity process between the free-stream turbulence and the laminar boundary layer, while for the turbulent state by the secondary instability. Note that it is only through conditional averaging that we can elucidate these important characteristics.

We note that in the experiments of [30] with and without boundary layer suction, the spanwise scale of the streaky structures was found to be the same, despite a two-fold reduction in the thickness of the boundary layer during suction. This led the authors to conclude that the length scale was determined by the receptivity process that was the same for both cases. This is in accordance with our findings. The present results are also consistent with those of Marxen and Zaki [28]. Using conditional averaging, they demonstrated the similarity of the first-order statistics between spots and fully turbulent flow at the late stages of transition (not in the baby spots).

The variation of $r_3^{(min)}/\delta^*$ is also shown in Fig. (10) with a black dotted line. The first point at $TRM1$ and the last one at the fully turbulent region have difference of 5%, but the two peaks are located at very different wall-normal distances. This figure also shows very clearly the coexistence of two length scales that correspond to the two different states of the flow.

Figure (15) shows similar behaviour in the (r_1, Y) plane, i.e. turbulent motions start near the top half of the boundary layer and then penetrate towards the wall; again this is consistent with the outer type secondary instability [19]. However the (r_1, Y) maps are distinctly different compared with the (r_3, Y) ones. In the latter, as we have just shown, the

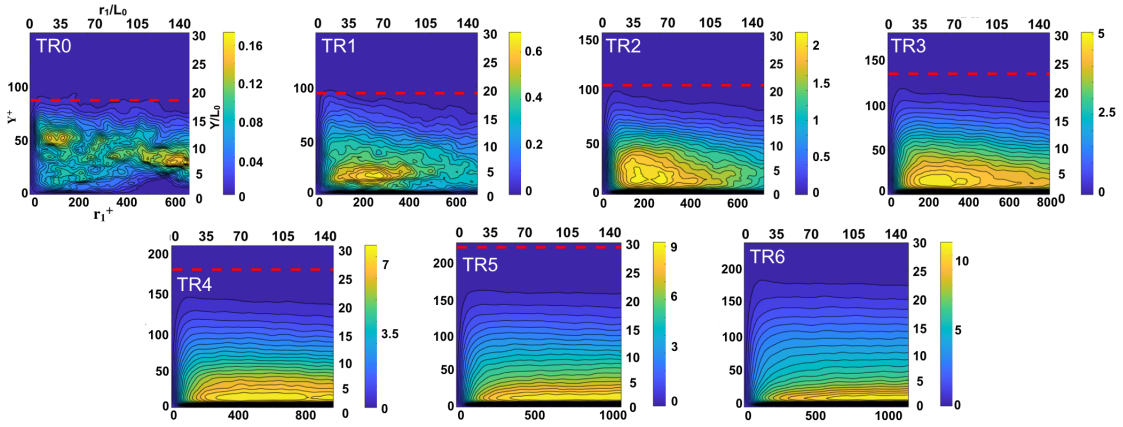

FIG. 15. Evolution of $\gamma^{(TT)}\langle du^2\rangle^{(TT)}$ on (r_1, Y) plane

r_3 separation corresponding to the maximum value of $\gamma^{(TT)}\langle du^2\rangle^{(TT)}$ was nearly constant throughout the transition process. From the (r_1, Y) maps however, it is evident that the separation r_1 corresponding to the maximum grows significantly, from $r_1 \approx 30L_0$ to $r_1 > 140L_0$. The peak area also becomes long and flat. There is a very clear physical explanation for this change of the length scale in the r_1 direction; it is due to the longitudinal growth of the structures within the turbulent spots. We explore this growth in the next section, by investigating the three-dimensional structure of the $\gamma^{(TT)}$ fields.

VI. TWO-POINT INTERMITTENCY FIELD $\gamma^{(TT)}$.

The intermittency $\gamma(X, Y)$ shown in Fig. (3) is a single-point, two dimensional, quantity and is not suitable for the analysis of the spot growth. On the other hand, the two-point intermittency field, $\gamma^{(TT)}$, contains a lot more information and, as we will see below, is a more appropriate quantity to use; for this reason, in this section, we focus on $\gamma^{(TT)}$.

As mentioned in section III, $\gamma^{(TT)}(X, Y; r_1, r_2, r_3)$ has a clear physical interpretation as the probability that both points $\vec{x}^{\pm} = \vec{X} \pm \vec{r}/2$ are located in turbulent patches or spots (but not necessarily the same spots). This probability is of course equal to the percentage of time that both points spend inside turbulent spots (averaged in the spanwise direction). It is clear that setting the separation distance to 0, i.e. $r_1 = r_2 = r_3 = 0$, results in $\gamma^{(TT)}(X, Y; 0, 0, 0) = \gamma(X, Y)$, i.e. the intermittency shown in figure 3.

Let's now fix the physical location (X, Y) and consider an iso-surface of constant $\gamma^{(TT)}(r_1, r_2, r_3)$ and the volume of fluid enclosed by this surface. Based on the aforemen-

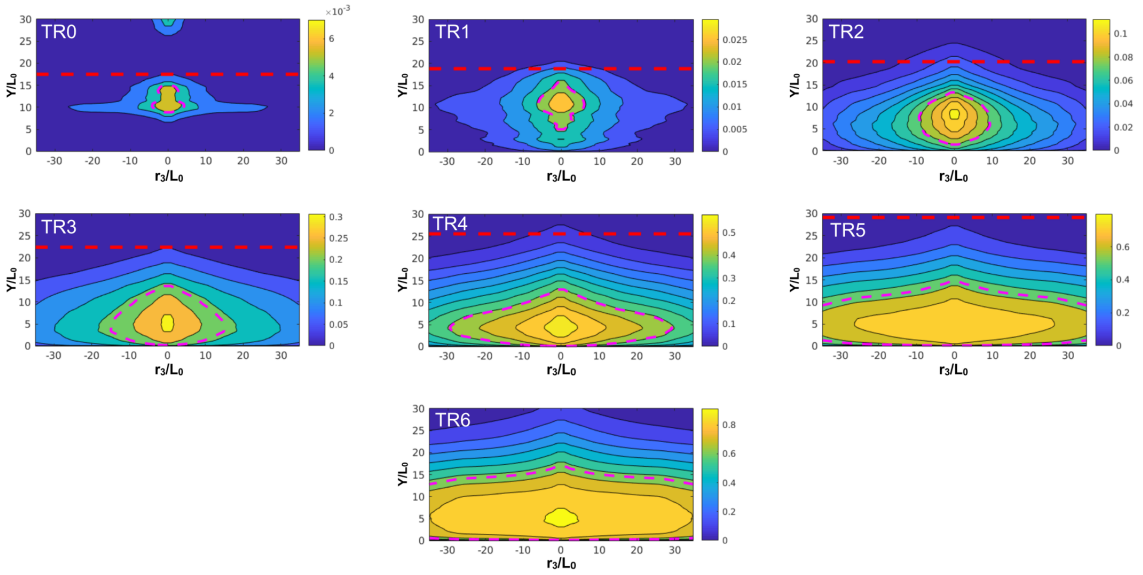

FIG. 16. Evolution of $\gamma^{(TT)}$ on (r_3, Y) plane; pinks isolines are defined as $\gamma^{(TT)} = 0.7\gamma^{(TT)}_{max}$

tioned interpretation, the fluid contained within this volume has a probability larger than or equal to the value of the iso-surface to be within one (or more) turbulent regions. This does not mean that this iso-surface indicates the shape of a turbulent spot. The proper way to identify the spot shape is to follow the tracking method described by [28]. Nevertheless, we would expect the volume enclosed within an isosurface of constant value to grow as the transition process develops, in a similar way as a spot grows.

In figure (16) we plot $\gamma^{(TT)}$ in the (r_3, Y) at different streamwise locations, i.e. we assume $r_1 = 0, r_2 = 0$. The distribution of $\gamma^{(TT)}$ for $r_3 = 0$ at each map corresponds to the intermittency shown in figure 3. In essence then, this figure shows the spanwise extent of the turbulent region at each streamwise location. The pink dash lines indicate the isoline $\gamma^{(TT)} = 0.7\gamma^{(TT)}_{max}$, where $\gamma^{(TT)}_{max}$ is the maximum value for the particular X location. Note that the plots are symmetric with respect to $r_3 = 0$. Indeed, $\gamma^{(TT)}$ does not depend on the sign of r_3; a negative value will simply swap the points $\vec{x}^{\pm}$ without changing $\gamma^{(TT)}$. The same is valid for all separations, i.e. $\gamma^{(TT)}(X, Y; r_1, r_2, r_3) = \gamma^{(TT)}(X, Y; -r_1, -r_2, -r_3)$.

The subplots in figure (16) are consistent with the scenario of the previous section. At $TR0$ the peak of the $\gamma^{(TT)}$ is located at $Y \approx 10 - 12$ and occupies a narrow region. It then moves in the wall-normal direction and expands horizontally in the r_3 direction. It is evident that the spot is forming at the top half of the boundary layer and then gradually fills the lower part. This corresponds to the top-down mechanism due to the outer type instability

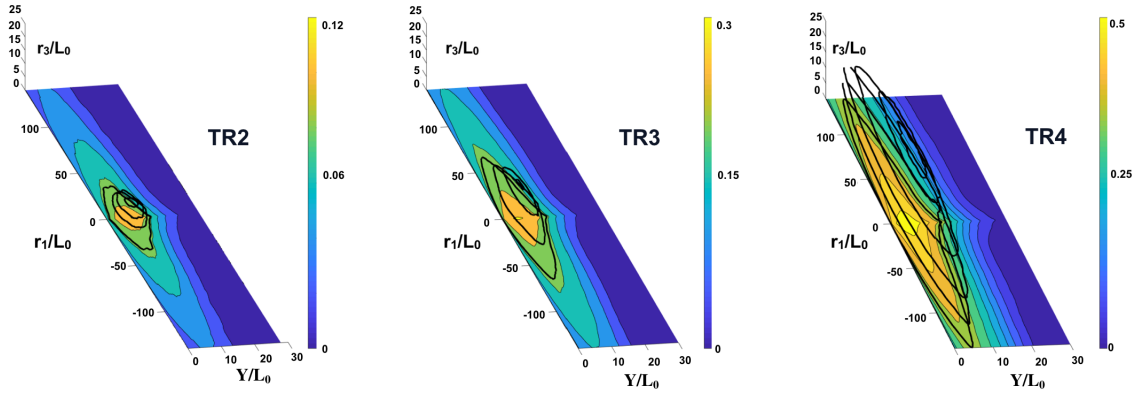

FIG. 17. Three dimensional plots of $\gamma^{(TT)}$ at streamwise locations $TR2, TR3, TR4$ (from left to right). The black isolines denote $\gamma^{(TT)} = 0.7\gamma^{(TT)}_{max}(r_3 = 0)$.

[27]. This top-to-bottom process can also be seen from the plots in the (r_1, Y) plane which is similar to the results in the(r_3, Y) plane and not shown here.

In figure (17) three-dimensional plots of $\gamma^{(TT)}$ in the (r_1, r_3, Y) domain are shown, for three streamwise locations $TR2, TR3, TR4$. Each plot was obtained by considering different values of r_3 and computing $\gamma^{(TT)}\ (r_1, Y; r_3)$ and stacking the results. For $TR2$ we considered the values $r_3 = 0, 3, 5, 6$, while for $TR3$ and $TR4$, $r_3 = 0, 5, 10, 12$ and $r_3 = 0, 5, 10, 12, 13, 15, 20, 21$ respectively. The black isolines are defined as $\gamma^{(TT)} = 0.7\gamma^{(TT)}_{max}$, where the $\gamma^{(TT)}_{max}$ is evaluated at $r_3 = 0$ (the black line on the bottom contour); the values of $\gamma^{(TT)}_{max}$ are $0.084, 0.21, 0.35$ for $TR2, TR3, TR4$ respectively. In these plots, a long volume can be observed with long streamwise length and much shorter spanwise extent. The size of the volume increases along with the streamwise direction, as expected. This feature explains the growth of r_1 separation observed earlier in figure 15.

VII. CONCLUSIONS

We use the second-order structure function of the streamwise velocity as a statistical tool to explore bypass transition due to free-stream turbulence in a flat plate boundary layer. In order to account for the intermittent formation of turbulent spots during the transition process, we derive a new decomposition of the time and spanwise averaged structure function in terms of conditionally-averaged quantities. The conditioning process is based on the instantaneous state of the flow at the two points that are used to define the structure

function. Three states are defined (a) both points are in turbulent patches (TT state), (b) both in laminar (LL state) and (c) one in laminar, the other in turbulent patch (LT state). The derived expressions generalise existing expressions for one-point statistics to two-point statistics. Such analysis sheds light into the process of bypass transition from a new perspective.

The conditional structure functions are calculated along the streamwise direction, at 8 locations, from the laminar region to fully turbulent. The results conditioned on the laminar state, indicate that the laminar streaks maintain their physical features even after mixing with the intermittent turbulent spots. Results conditioned on turbulent state show that the initial turbulent motion starts near the boundary layer edge, consistent with the so-called outer secondary instability. Again the spanwise length scale of the turbulent spots is retained throughout the transition, but the streamwise increases significantly. It is only through the use of conditional statistics that these features can be clearly elucidated. The two-point intermittency $\gamma^{(TT)}$ was also examined. We noticed the growth in the volume of fluid enclosed by isosurfaces of this quantity along the both directions. The growth was observed mostly along the r_1 separation, indicative of the large increase of the length of the turbulent spots.

We close this section with some thoughts on future perspectives. Recall that $\langle du^2 \rangle + \langle dv^2 \rangle + \langle dw^2 \rangle$ (where $\langle du^2 \rangle$ makes the largest contribution) represents the energy contained within an eddy of size $|\vec{r}|$ which is centred at point $\vec{X} = (X, Y, Z)$. Its evolution is governed by the Karman-Howarth equation, which is valid for general inhomogeneous flows, so it is applicable to the present case. Using the database generated, we can compute the rate of energy transfer between structures of different length scales, and use this information to draw the energy flow paths that determine the growth of turbulent spots. Furthermore, it is well known that spots merge to form larger spots. This implies an inverse energy transfer process, i.e. energy flowing from small to large scales, in contrast to the standard view of forward cascade (energy from large to small scales). Is there a competition between extracting energy from the mean flow (forward cascade) and from the inverse cascade process? What is the relative contribution of these two mechanisms? Future work in this direction will help to answer such questions.

VIII. ACKNOWLEDGMENT

The authors would like to thank the UK Turbulence Consortium for providing computational time in the UK supercomputing facility ARCHER via the EPSRC grant EP/R029326/1. The first author would like also to acknowledge the financial support from the Department of Aeronautics and the Imperial College-CSC scholarship.

Appendix A: Convergence of $\langle du^2 \rangle$ with the number of samples.

Figure 18 shows two examples of convergence of $\langle du^2 \rangle$ with increasing number of samples. The location considered is at the fully turbulent region, $(X - X_0)/L_0 = 2415$, and the wall-normal distance is fixed to $Y/L_0 = 1.3$. The top panel is for a small streamwise separation $r_1/L_0 = 5$ and the bottom panel is for larger separation, $r_1/L_0 = 100$.

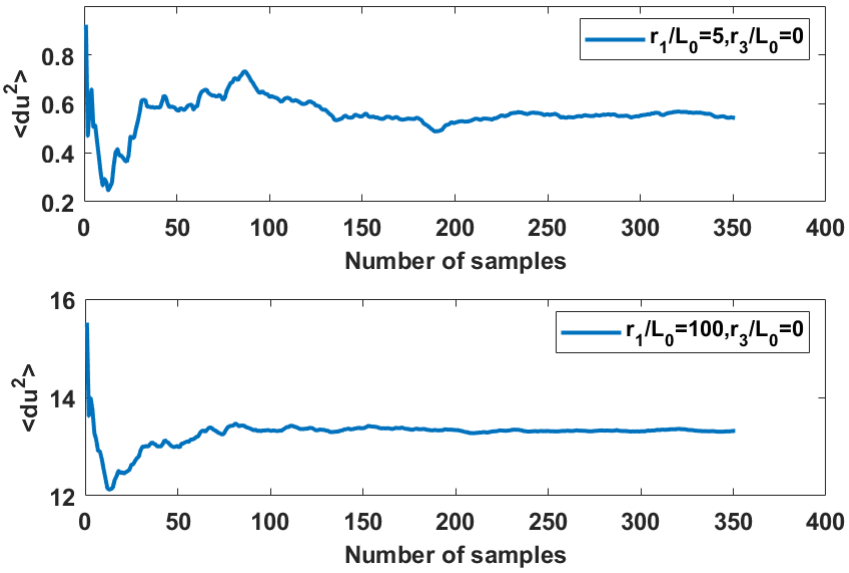

FIG. 18. Running average of $\langle du^2 \rangle$ versus the number of samples at a streamwise location inside the fully turbulent region, $(X - X_0)/L_0 = 2415$, at fixed height $Y/L_0 = 1.3$ and two different r_1 separations.

[1] M. V. Morkovin, On the many faces of transition, in *Viscous drag reduction* (Springer, 1969) pp. 1–31.

[2] P. Klebanoff, Effect of free-stream turbulence on a laminar boundary layer, in *Bulletin of the American Physical Society*, Vol. 16 (1971) pp. 1323–+.

[3] K. Westin, A. Boiko, B. Klingmann, V. Kozlov, and P. Alfredsson, Experiments in a boundary layer subjected to free stream turbulence. part 1. boundary layer structure and receptivity, Journal of Fluid Mechanics **281**, 193 (1994).

[4] M. Matsubara and P. H. Alfredsson, Disturbance growth in boundary layers subjected to free-stream turbulence, Journal of fluid mechanics **430**, 149 (2001).

[5] J. H. Fransson, M. Matsubara, and P. H. Alfredsson, Transition induced by free-stream turbulence, Journal of Fluid Mechanics **527**, 1 (2005).

[6] R. Jacobs and P. Durbin, Simulations of bypass transition, Journal of Fluid Mechanics **428**, 185 (2001).

[7] L. Brandt, P. Schlatter, and D. S. Henningson, Transition in boundary layers subject to free-stream turbulence, Journal of Fluid Mechanics **517**, 167 (2004).

[8] T. A. Zaki and P. A. Durbin, Mode interaction and the bypass route to transition, Journal of Fluid Mechanics **531**, 85 (2005).

[9] V. Ovchinnikov, M. M. Choudhari, and U. Piomelli, Numerical simulations of boundary-layer bypass transition due to high-amplitude free-stream turbulence, Journal of Fluid Mechanics **613**, 135 (2008).

[10] J. Hunt and P. Durbin, Perturbed vortical layers and shear sheltering, Fluid Dynamics Research **24**, 375 (1999).

[11] T. A. Zaki and S. Saha, On shear sheltering and the structure of vortical modes in single-and two-fluid boundary layers, Journal of Fluid Mechanics **626**, 111 (2009).

[12] J. M. Kendall, Studies on laminar boundary-layer receptivity to freestream turbulence near a leading edge, in *Boundary layer stability and transition to turbulence* (1991) pp. 23–30.

[13] O. M. Phillips, Shear-flow turbulence, Annual Review of Fluid Mechanics **1**, 245 (1969).

[14] L. Brandt, The lift-up effect: the linear mechanism behind transition and turbulence in shear flows, European Journal of Mechanics-B/Fluids **47**, 80 (2014).

[15] M. Landahl, A note on an algebraic instability of inviscid parallel shear flows, Journal of Fluid Mechanics **98**, 243 (1980).

[16] T. A. Zaki and P. A. Durbin, Mode interaction and the bypass route to transition, J. Fluid Mech. **531**, 85 (2005).

[17] P. A. Durbin, Perspectives on the phenomenology and modeling of boundary layer transition, Flow, Turbulence and Combustion **99**, 1 (2017).

[18] P. Schlatter, L. Brandt, H. De Lange, and D. S. Henningson, On streak breakdown in bypass transition, Physics of fluids **20**, 101505 (2008).

[19] N. J. Vaughan and T. A. Zaki, Stability of zero-pressure-gradient boundary layer distorted by unsteady klebanoff streaks, Journal of Fluid Mechanics **681**, 116 (2011).

[20] M. Hack and T. Zaki, Streak instabilities in boundary layers beneath free-stream turbulence, Journal of Fluid Mechanics **741**, 280 (2014).

[21] H. Emmons, The laminar-turbulent transition in a boundary layer-part i, Journal of the Aeronautical Sciences **18**, 490 (1951).

[22] I. Wygnanski, M. Sokolov, and D. Friedman, On a turbulent 'spot' in a laminar boundary layer, Journal of Fluid Mechanics **78**, 785 (1976).

[23] A. Perry, T. Lim, and E. Teh, A visual study of turbulent spots, Journal of Fluid Mechanics **104**, 387 (1981).

[24] E. C. Itsweire and C. W. Van Atta, An experimental investigation of coherent substructures associated with turbulent spots in a laminar boundary layer, Journal of Fluid Mechanics **148**, 319 (1984).

[25] R. J. Anthony, T. V. Jones, and J. E. LaGraff, High frequency surface heat flux imaging of bypass transition, in *ASME Turbo Expo 2004: Power for Land, Sea, and Air* (American Society of Mechanical Engineers, 2004) pp. 185–195.

[26] X. Wu, P. Moin, J. M. Wallace, J. Skarda, A. Lozano-Durán, and J.-P. Hickey, Transitional–turbulent spots and turbulent–turbulent spots in boundary layers, Proceedings of the National Academy of Sciences **114**, E5292 (2017).

[27] K. P. Nolan and T. A. Zaki, Conditional sampling of transitional boundary layers in pressure gradients, Journal of Fluid Mechanics **728**, 306 (2013).

[28] O. Marxen and T. A. Zaki, Turbulence in intermittent transitional boundary layers and in turbulence spots, Journal of Fluid Mechanics **860**, 350 (2019).

[29] B. Eckhardt, K. Marzinzik, and A. Schmiegel, Transition to turbulence in shear flows, in *A perspective look at nonlinear media* (Springer, 1998) pp. 327–338.

[30] J. H. M. Fransson and P. H. Alfredsson, On the disturbance growth in an asymptotic suction boundary layer, Journal of Fluid Mechanics **482**, 51–90 (2003).

[31] K. J. A. Westin, A. V. Boiko, B. G. B. Klingmann, V. V. Kozlov, and P. H. Alfredsson, Experiments in a boundary layer subjected to free stream turbulence. part 1. boundary layer structure and receptivity, Journal of Fluid Mechanics **281**, 193–218 (1994).

[32] P. Andersson, M. Berggren, and D. S. Henningson, Optimal disturbances and bypass transition in boundary layers, Physics of Fluids **11**, 134 (1999).

[33] P. Luchini, Reynolds-number-independent instability of the boundary layer over a flat surface: optimal perturbations, Journal of Fluid Mechanics **404**, 289–309 (2000).

[34] P. A. Davidson, *Turbulence: an introduction for scientists and engineers* (Oxford University Press, 2015).

[35] R. J. Hill, Equations relating structure functions of all orders, Journal of Fluid Mechanics **434**, 379 (2001).

[36] R. J. Hill, Exact second-order structure-function relationships, Journal of Fluid Mechanics **468**, 317 (2002).

[37] N. Marati, C. Casciola, and R. Piva, Energy cascade and spatial fluxes in wall turbulence, Journal of Fluid Mechanics **521**, 191 (2004).

[38] F. A. Portela, G. Papadakis, and J. Vassilicos, The turbulence cascade in the near wake of a square prism, Journal of Fluid Mechanics **825**, 315 (2017).

[39] R. Gomes-Fernandes, B. Ganapathisubramani, and J. Vassilicos, The energy cascade in near-field non-homogeneous non-isotropic turbulence, Journal of Fluid Mechanics **771**, 676 (2015).

[40] S. B. Pope, *Turbulent flows* (Cambridge University Press, 2001).

[41] I. Paul, G. Papadakis, and J. C. Vassilicos, Genesis and evolution of velocity gradients in near-field spatially developing turbulence, Journal of Fluid Mechanics **815**, 295–332 (2017).

[42] D. Xiao and G. Papadakis, Nonlinear optimal control of bypass transition in a boundary layer flow, Physics of Fluids **29**, 054103 (2017).

[43] D. Xiao and G. Papadakis, Nonlinear optimal control of transition due to a pair of vortical perturbations using a receding horizon approach, Journal of Fluid Mechanics **861**, 524–555 (2019).

[44] P. Roach, The influence of a turbulent free-stream on zero pressure gradient transitional boundary layer development: Part 1. test cases T3A and T3B, in *ERCOFTAC Workshop, Lausanne* (1990).

[45] G. Taylor, *Some recent developments in the study of turbulence* (Wiley, New York, 1939).

[46] N. Otsu, A threshold selection method from gray-level histograms, IEEE transactions on systems, man, and cybernetics **9**, 62 (1979).

[47] R. Narashimha, On the distribution of intermittence in the transition region of a boundary layer, Journal of Aeronautical Science **24**, 711 (1957).

[48] R. Narasimha, The laminar-turbulent transition zone in the boundary layer, Progress in Aerospace Sciences **22**, 29 (1985).

[49] P. A. Davidson, T. B. Nickels, and P.-Å. Krogstad, The logarithmic structure function law in wall-layer turbulence, Journal of Fluid Mechanics **550**, 51–60 (2006).

[50] N. Saikrishnan, E. De Angelis, E. K. Longmire, I. Marusic, C. M. Casciola, and R. Piva, Reynolds number effects on scale energy balance in wall turbulence, Physics of Fluids **24**, 015101 (2012).